HHS Public Access

Author manuscript

Atmos Environ (1994). Author manuscript; available in PMC 2022 January 15.

Published in final edited form as:

Atmos Environ (1994). 2021 January 15; 245: . doi:10.1016/j.atmosenv.2020.117988.

Iron Speciation in Particulate Matter ($PM_{2.5}$) from Urban Los Angeles Using Spectro-microscopy Methods

Ajith Pattammattel[1], **Valerie J. Leppert**[2], **Paul Aronstein**[3], **Matthew Robinson**[2], **Amirhosein Mousavi**[4], **Constantinos Sioutas**[4], **Henry Jay Forman**[5], **Peggy A. O'Day**[1,3,*]

[1]Sierra Nevada Research Institute and School of Natural Sciences, University of California, Merced, 95343, USA

[2]School of Engineering, University of California, Merced, 95343, USA

[3]Environmental Systems Program, University of California, Merced, 95343, USA

[4]Viterbi School of Engineering, University of Southern California, Los Angeles, USA

[5]Leonard Davis School of Gerontology, University of Southern California, Los Angeles, USA

Abstract

The speciation, oxidation states, and relative abundance of iron (Fe) phases in $PM_{2.5}$ samples from two locations in urban Los Angeles were investigated using a combination of bulk and spatially resolved, element-specific spectroscopy and microscopy methods. Synchrotron X-ray absorption spectroscopy (XAS) of bulk samples *in situ* (i.e., without extraction or digestion) was used to quantify the relative fractions of major Fe phases, which were corroborated by spatially resolved spectro-microscopy measurements. Ferrihydrite (amorphous Fe(III)-hydroxide) comprised the largest Fe fraction (34-52%), with hematite (α-Fe_2O_3; 13-23%) and magnetite (Fe_3O_4; 10-24%) identified as major crystalline oxide components. An Fe-bearing phyllosilicate fraction (16-23%) was fit best with a reference spectrum of a natural illite/smectite mineral, and metallic Fe(0) was a relatively small (2-6%) but easily identified component. Sizes, morphologies, oxidation state, and trace element compositions of Fe-bearing PM from electron microscopy, electron energy loss

*corresponding author poday@ucmerced.edu.

Author Credit Statement

Ajith Pattammattel: Methodology, Validation, Formal analysis, Investigation, Writing - Original Draft, Writing - Review & Editing, Visualization. Valerie J. Leppert: Conceptualization, Methodology, Validation, Writing - Review & Editing, Supervision, Funding acquisition, Project administration. Paul Aronstein: Investigation, Data Curation, Writing - Review & Editing. Matthew Robinson: Investigation. Amirhosein Mousavi: Methodology, Investigation, Writing - Review & Editing. Constantinos Sioutas: Methodology, Resources, Writing - Review & Editing. Henry Jay Forman: Conceptualization, Writing - Review & Editing, Supervision, Funding acquisition, Project administration. Peggy A. O'Day: Conceptualization, Methodology, Validation, Writing - Original Draft, Writing - Review & Editing, Supervision, Funding acquisition, Project administration.

Declaration of competing interest

The authors declare that they have no known competing financial interests or personal relationships that could have appeared to influence the work reported in this paper.

Declaration of interests

The authors declare that they have no known competing financial interests or personal relationships that could have appeared to influence the work reported in this paper.

spectroscopy (EELS), and scanning transmission X-ray microscopy (STXM) revealed variable and heterogeneous mixtures of Fe species and phases, often associated with carbonaceous material with evidence of surface oxidation. Ferrihydrite (or related Fe(III) hydroxide phases) was ubiquitous in PM samples. It forms as an oxidation or surface alteration product of crystalline Fe phases, and also occurs as coatings or nanoparticles dispersed with other phases as a result of environmental dissolution and re-precipitation reactions. The prevalence of ferrihydrite (and adsorbed Fe(III) has likely been underestimated in studies of ambient PM because it is non-crystalline, non-magnetic, more soluble than crystalline phases, and found in complex mixtures. Review of potential sources of different particle types suggests that the majority of Fe-bearing PM from these urban sites originates from anthropogenic activities, primarily abrasion products from vehicle braking systems and engine emissions from combustion and/or wear. These variable mixtures have a high probability for electron transfer reactions between Fe, redox-active metals such as copper, and reactive carbon species such as quinones. Our findings suggest the need to assess biological responses of specific Fe-bearing phases both individually and in combination to unravel mechanisms of adverse health effects of particulate Fe.

Graphical Abstract

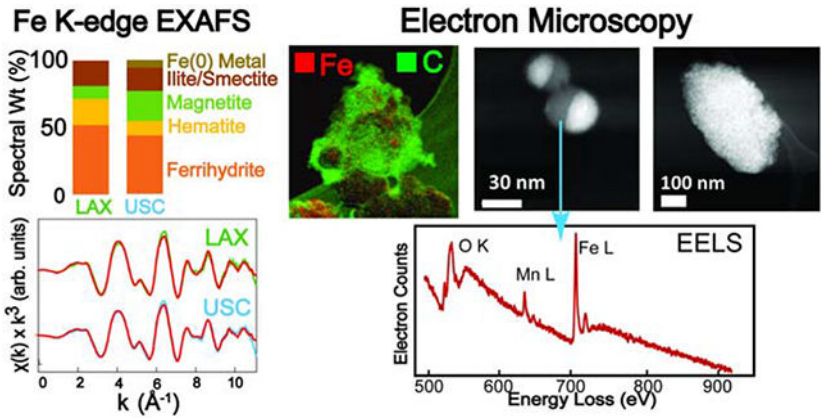

Keywords

$PM_{2.5}$; iron speciation; X-ray absorption spectroscopy; electron energy loss spectroscopy; non-exhaust emissions; exhaust emissions

1. Introduction

Particulate matter (PM) pollution is responsible for over 4 million deaths per year around the world (WHO, 2016). The World Health Organization (WHO) estimated that more than 90% of the world's population lives with polluted air, which is associated with increased risks of cardiopulmonary disease and stroke, and increased vulnerability to inflammation-associated pathologies such as respiratory diseases and lung cancers (Anderson et al., 2012; EPA, 2009; WHO, 2016). Although underlying mechanisms remain to be elucidated, it is thought that generation of reactive oxygen species and oxidative stress play a central role in the pathogenesis of health disorders associated with ambient particles of $PM_{2.5}$ or less (Buzea et

al., 2007; Tao et al., 2003). Metals such as Fe that are commonly found in multiple oxidation states may have a disproportionate effect in cellular response because of their ability to participate in oxidation of macromolecules, thereby altering membrane and signaling functions and resulting in oxidative stress and associated inflammation (Block and Calderon-Garciduenas, 2009; Charrier et al., 2014; See et al., 2007).

Outdoor air PM separated by aerodynamic diameter (typically PM_{10} or $PM_{2.5}$) and measured by particle concentration per volume has often shown poor correlation with mortality or morbidity rates, which suggests that the physical and chemical identity of PM strongly influences health impacts (Cassee et al., 2013). Chemical components in PM are typically classified into organic and inorganic fractions. Organic compounds in PM are a complex mixture of a large number of volatile to semi-volatile organic molecules and polyaromatic hydrocarbons of primary or secondary origin with a range of potential biological activity (Fine et al., 2004). Elemental carbon (C) is monitored as a proxy for automobile emissions and other types of fossil fuel combustion (Schauer et al., 1996). The inorganic fraction in PM is dominated by soluble ionic salts (sulfate, nitrate, ammonium, sodium, and potassium) that are typically measured by aqueous extraction of the PM sample and ion chromatography (Chow and Watson, 1999). The remaining elements usually constitute a relatively small mass fraction of $PM_{2.5}$ samples. Bulk elemental analyses is performed by acid digestion of the sample and measurement of individual element concentrations by, for example, inductively coupled plasma-mass spectrometry (ICP-MS) or energy dispersive X-ray fluorescence (ED-XRF) (Mazzei et al., 2008). Compared with bulk analyses, few studies have examined the chemical speciation or solid-phase hosts of metal elements in PM *in situ* (i.e., without extraction or digestion). Identifying specific metal species in PM is beneficial to understanding its biological activity after inhalation and potential impact on general and susceptible human populations.

Iron (Fe) is the most abundant transition metal in PM. Sources include a variety of anthropogenic and natural processes, and Fe phases are susceptible to atmospheric reprocessing (Gonet and Maher, 2019; Shi et al., 2012). The abundance and identity of Fe species may vary with PM size fraction,sample location, and weather at the time of collection, and the ability to detect particular Fe species depends on the analytical, microscopic, or spectroscopic method employed. Element-specific methods such as synchrotron X-ray absorption spectroscopy (XAS) and spectro-microscopy, Mössbauer spectroscopy, and electron spectro-microscopy techniques such as electron energy loss spectroscopy (EELS) or electron probe X-ray microanalysis (EMPA) are particularly useful for identifying specific Fe phases in a chemically complex matrix such as PM, although each technique has particular strengths and weaknesses. Several studies have applied XAS at either the Fe K- or L- edge to estimate fractions of Fe oxidation states and possible host minerals in PM. Using Fe L_3/L_2-edge X-ray absorption near edge structure (XANES) analysis, the fraction of Fe(III) in size-fractioned (<10 μm) PM samples from three urban sites (in IL, CA, and WI, USA) was estimated at > 60% but the Fe-bearing phases were not determined (Majestic et al., 2007). A study of urban PM samples from New Jersey (USA) used Fe K-edge microfocused (μ-) XANES to characterize mixtures of Fe phases, which contained magnetite (Fe_3O_4) and other Fe(III)-(hydr)oxide minerals that could not be conclusively identified (Elzinga et al., 2011). Iron speciation in particles from $PM_{2.5}$

samples collected from urban and rural sites in Georgia (USA) were studied with Fe μ-XANES, and relative Fe(II)/Fe(III) fractions were estimated from analysis of the energy position of the pre-edge centroid (Oakes et al., 2012). The Fe(II) fraction was estimated at 5-35% (average 25%) and element correlations with Fe were used to infer possible host minerals as Fe-oxides with Al substitution and Fe-bearing aluminosilicates. An XAS study of PM (0.5-40 μm) collected from Western Africa (Niger in 2006) showed that 40-70% of the elemental Fe in PM is present as Fe(III), with the Fe(III)-oxide fraction dominated by goethite (α-FeOOH) and to a lesser extent hematite (α-Fe_2O_3) (Formenti et al., 2014). Samples of different PM sizes collected in central Italy and examined by XAS showed evidence for Fe(III)-oxide and aluminosilicate phases from Saharan dust at a rural site, whereas PM samples from two urban sites showed evidence of an Fe spinel-type phase linked to steel production emissions (Petroselli et al., 2019).

Other characterization methods such as Mössbauer spectroscopy and Raman microspectroscopy have been used to identify specific Fe phases. A Fe^{57}-Mössbauer spectroscopy and X-ray fluorescence (XRF) study of PM (<2 μm) collected from the Belo Horizonte metropolitan area (Brazil) reported that hematite and goethite were major Fe species in PM (Tavares et al., 2014). Another Mössbauer spectroscopy investigation, complemented with magnetic measurements, on nanoparticle PM (<0.03 μm) from Munich (Germany) identified maghemite (γ-Fe_2O_3) and metallic Fe as major species, which were attributed to local input from railroads (Muxworthy et al., 2002). Similarly, metallic Fe, magnetite, and hematite were reported in airborne subway particles (PM_{10}) in Seoul (South Korea) using a combination of EMPA and Raman microspectroscopy (Eom et al., 2013), and these phases were identified in PM of other subway and rail systems (Moreno et al., 2018). The presence of magnetite nanoparticles in urban PM was reported in several studies, and related to automobile emissions, engine wear, and brake system wear (Gonet and Maher, 2019; Kukutschová and Filip, 2018). Evidence from spatially resolved electron energy loss spectroscopy (EELS) was used to propose that wüstite (FeO), magnetite, hematite, and maghemite constituted Fe in road dust (0.3-0.6 μm) collected from areas of Bristol and Newcastle (UK) (Sanderson et al., 2016). Goethite, magnetite, hematite, ferrihydrite (amorphous $Fe(OH)_3$), and Fe-rich coal fly ash were identified in nanoscale dust particles (<100 nm) collected from Shanghai (China) using electron microscopy and selected-area electron diffraction (SAED) (Yang et al., 2016).

The variability in Fe speciation reported in the literature probably reflects both the complexity associated with mixtures of phases and species in PM of different size fractions from different localities, as well as the ability, sensitivity, and accuracy of individual techniques to determine characteristics such as oxidation state, chemical bonding, or mineral phase. For example, techniques such as Mössbauer spectroscopy or XAS applied to bulk sample characterization provide an average of all chemical bonding environments of the target element but are not sensitive to minor components. For XAS in particular, results can be inconclusive if few comparative reference spectra are used to identify phases, data quality is poor due to low sample mass, or only XANES rather than full extended X-ray absorption fine structure (EXAFS) spectra are analyzed. Likewise, different types of measurements of magnetic susceptibility are very sensitive to Fe magnetic phases, particularly magnetite, maghemite, hematite, and Fe(0) metal, but insensitive to non-magnetic phases and difficult

to apply quantitatively to the determination of specific Fe phases in mixtures (Hofman et al., 2017; Roberts et al., 2014). Many prior studies that applied spectroscopic characterizations or analyses by X-ray diffraction examined larger size fractions such as PM_{10} or samples of mixed particle sizes, rather than $PM_{2.5}$ or finer fractions. Spatially resolved methods, in particular electron microscopy-based methods, provide high spatial resolution imaging of individual particles, but obtaining quantitative chemical or structural information about individual particles can be difficult, and determining relative abundances of species or phases requires statistical averaging of many measurements.

In order to take advantage of the strengths afforded by using multiple characterization methods, we applied an integrated approach in this study by employing a combination of bulk and spatially resolved methods to determine qualitative and quantitative Fe speciation in urban $PM_{2.5}$ collected from two locations in Los Angeles (CA, USA). We employed element-specific X-ray spectroscopy and electron spectro-microscopy analyses, and particle imaging methods at different scales (from micrometer to nanometer), to estimate relative fractions, oxidation states, distribution, and association of Fe-bearing phases and species. These analyses and interpretation of their potential sources provide a more complete picture of the relative abundances and types of anthropogenic and geogenic Fe in respirable PM that have potential impacts for human health in urban settings.

2. Materials and methods

2.1 Materials

Stainless steel nanoparticles (<100 nm, 316L) were purchased from US Research Nanomaterials, Inc. (Houston, TX, USA). Iron powder was collected by grinding Fe metal in mineral oil. Magnetite nanoparticles (10 nm) and ferrihydrite were synthesized according to published protocols (Schwertmann and Cornell, 2000; Yazdani and Seddigh, 2016). Monarch 120 C nanoparticles (CNP) were obtained from Cabot, Inc. and oxidized with concentrated (15 M HNO_3) according to a published protocol (Moreno-Castilla et al., 1995). A list of reference spectra and their sources used for XAS analyses are given in Tables S1 and S2 (supplementary materials).

2.2 $PM_{2.5}$ sample collection

Time-integrated PM sampling was conducted continuously (24 hours) on a weekly basis. Sampling conditions and instrumentation were reported previously (Shirmohammadi et al., 2017a; Shirmohammadi et al., 2017b). Los Angeles International Airport (LAX) $PM_{2.5}$ samples were collected at the South Coast Air Quality Management District's Hastings monitoring site located adjacent to the airport. USC $PM_{2.5}$ samples were collected at the Particle Instrumentation Unit of the University of Southern California located about 3 km south of downtown Los Angeles and immediately downwind of the I-110 freeway. At each site, Sioutas™ Personal Cascade Impactor Samplers (PCISs) (SKC, Inc., Eighty Four, PA, USA) (Misra et al., 2002) operating at a flow rate of 9 liters per minute were installed for size-segregated PM collection. PCISs were loaded with 37 mm PTFE (Teflon) filters (Pall Life Sciences, 3-μm pore, Ann Arbor, MI). Table 1 shows sampling periods and masses of material collected.

2.3 Bulk chemical analysis

Replicate filters from LAX1 and USC2 collection (Table 1) were used for bulk chemical analysis. Organic and elemental C as well as trace element and metals analysis were conducted by the University of Wisconsin, Madison and the Wisconsin State Laboratory of Hygiene. Replicates of USC1 and LAX2, collected on a 25 mm quartz filter, were used for elemental C (EC) and organic C (OC) analysis, following the Thermal Optical Transmission (TOT) method from National Institute for Occupational Safety and Health (NIOSH) (Birch and Cary, 1996). Elemental analysis was conducted by digestion of the Teflon filter in acid (2.00 mL nitric acid + 0.500 mL hydrochloric acid + 0.2 mL hydrofluoric acid) and microwave-assisted digestion. PM digests were diluted 1:3 for ICP-MS analysis using a magnetic-sector ICP-MS (Thermo-Finnigan Element 2) as discussed in (Shirmohammadi et al., 2017b). Analytical uncertainty included the standard deviation of triplicate analyses on each sample, blank subtraction (standard deviation of 4-5 method blanks from each batch), and digestion recovery (long-term standard deviation of SRM recoveries).

2.4 X-ray absorption spectroscopy

Bulk XANES and EXAFS spectra were collected at the Stanford Synchrotron Radiation Lightsource (SSRL) beamline 4-1. Teflon filters with PM as received and without modification were mounted onto Al-holders, sealed using sulfur free tape, and held at liquid N_2 temperature to prevent reaction with the X-ray beam and potential oxidation state changes during data collection. Spectra were collected using a 1 x 4 mm beam size generated from a Si(220) monochromator and successive scans on a sample showed no spectral changes that would indicate beam damage. The monochromator was detuned by ~50% from maximum energy for rejection of high-order harmonic reflections. Energy for the Fe K-edge was calibrated using the first inflection on the absorption edge of Fe metal foil, set at 7112.0 eV. X-ray fluorescence was collected after reducing the background with a Mn filter (Z-1) and soller slits that were placed between the sample and a solid state Ge detector (32 elements, Canberra). Four EXAFS spectra (to k ~12 $Å^{-1}$) were collected and averaged for each sample.

Pre-edge correction, normalization, and linear combination (LC) fitting of the XANES, EXAFS and μ-XANES were performed using the Athena program (Ravel and Newville, 2005). For bulk XAS spectra, the XANES and EXAFS regions of the spectra were separated, and background subtraction and normalization were optimized for each region in order to closely match the normalization of the reference spectra. A previously published spectral library of known natural and synthetic Fe compounds was used for LC fits (O'Day et al., 2004) (Table S1). Initially, the entire library was used to screen unknown spectra for matches to major classes of compounds, which included Fe(II) and Fe(III) oxide, hydroxide, phyllosilicate, sulfate, sulfide, carbonate, and phosphate phases; Fe(0) metal; Fe-organic compounds; and spectra of Fe adsorbed to carbon and silica (Table S1). Once satisfactory fits were obtained and the major components identified, a smaller set of reference spectra from the library were used to determine the final best LC fits (Table S2) and to conduct sensitivity tests for statistical significance. Fits were performed without normalization; component fractions are reported as both raw fits and normalized to 100%. See supplementary material for details of the XAS data analysis.

Spatially resolved μ-XRF maps and μ-XANES spectra were collected at SSRL beamline 2-3, using a ~2 μm size beam (Kirkpatrick-Baez mirror geometry). XRF maps (λ_{ex} =13050 eV, 25 s dwell time) were collected at room temperature using a Vortex 2X fluorescence detector. Samples were imaged directly on the Teflon filter without modification or after smearing particles with a polypropylene spatula on the filter to reduce aggregation and spread them out. No differences in results were observed with the two preparation methods. XANES spectra were collected on particles with sufficient Fe fluorescence counts. Three or more spectra were collected from each particle and averaged. Data analysis was performed using SIXpack, an X-ray microanalysis toolkit (Webb, 2005), and LC fits were done on XANES spectra using Athena as described above for bulk XAS.

2.5 Electron microscopy and electron energy-loss spectroscopy (EELS)

Grids for transmission electron microscopy (TEM) were prepared from an aqueous dispersion of the PM prepared by sonication of the Teflon filter for 5 minutes in Milli-Q water and drop casted (2 μL) onto a 400-mesh holey carbon Cu grid (Ted Pella, Redding, CA, USA). The grid was dried in a vacuum desiccator for at least 12 hours before imaging. High resolution TEM (HR-TEM) images were collected on a JEOL JEM-2011 transmission electron microscope (Peabody, MA, USA) equipped with a LaB_6 filament and operated at 200 kV accelerating voltage. Scanning transmission electron microscopy (STEM) images coupled with energy-dispersive X-ray spectrometry (EDXS) were collected on a Philips CM200/FEG instrument operated at 200 kV and equipped with an Oxford INCA detector with an energy resolution of 136 eV for Mn K-α radiation. STEM-electron energy-loss spectroscopy (EELS) and energy filtered-transmission electron microscopy images (EFTEM) were collected using a Gatan imaging filter (GIF) on an F20 UT Tecnai microscope (200 kV) equipped with a high-angle annular dark-field (HAADF) detector. EFTEM was acquired by collecting bright field TEM images at the C K- and Fe L- edge energies, and the pre-edge/post-edge normalization was applied by the data collection software. EELS data was processed using Gatan Digital Micrograph program (GMS3 Suite) provided by Gatan Inc. The L_3/L_2 ratio was estimated by the method described by van Aken (van Aken and Liebscher, 2002). Reference spectra were collected for stainless steel nanoparticles (Fe(0)), ilmenite ($FeTiO_3$), magnetite (Fe_3O_4), hematite (α-Fe_2O_3), and ferrihydrite (amorphous $Fe(OH)_3$) (see Fig. S1, Table S3, and supplementary material for details of EELS data collection and analysis). The L_3/L_2 ratio estimated for these compounds was similar to previously reported values (±0.3) (Chen et al., 2007; Jasinski et al., 2006).

2.6 Scanning transmission X-ray microscopy (STXM)

In order to obtain spatially resolved information about C, O, and Fe speciation in PM, STXM data were collected at the Canadian Light Source (CLS Beamline 10ID-1, Saskatoon, Canada). PM samples were dispersed in ultrapure water (18.2 MΩ·cm, Milli-Q), and 2 μL was deposited on a 100 nm-thick SiN membrane (Norcada, Canada), and air dried. A Fresnel Zone plate was used to achieve ~30 nm spatial resolution. Data were collected with the sample held at ~125 mm Hg atmosphere at room temperature. Image stacks at different energies for the C K-, O K-, and Fe L- edges were collected in transmission mode (see Table

S4). The MANTiS 2.3.02 program was used for background (I_0) subtraction, alignment, principle component analysis (PCA), and cluster analysis of the stacks (Lerotic et al., 2014).

3. Results

3.1 Elemental analysis

Quantitative bulk chemical analysis of $PM_{2.5}$ samples (Fig. 1A) showed that both locations had similar elemental composition, except for a higher Na concentration in the LAX sample. At both sites, Fe was the most abundant transition metal (LAX1: 39 μg Fe/ mg or 101 ng Fe/m^3; USC2: 42 μg Fe/mg or 202 ng Fe/m^3). More than 30% of the PM was composed of carbonaceous materials, measured as organic or elemental C. Total C concentrations were higher in the LAX than the USC sample, and were dominated by organic C (Fig. 1B). Elemental C was higher in the USC sample compared to the LAX sample. Comparison of chemical data of our samples to $PM_{2.5}$ filter data from the Speciation Trends Network (STN) established by the USEPA collected in central Los Angeles over a similar time period, and with compositions of the $PM_{0.25}$ fraction from the LAX and USC sites from a prior complementary study (Shirmohammadi et al., 2018), shows similar concentrations for trace elements, metals, OC, and EC (see Fig. S2 and discussion in supplementary material). In general, the elemental composition indicates that our samples are adequately representative of the atmospheric $PM_{2.5}$ composition in the study area.

3.2 Bulk X-ray absorption spectroscopy

The total bulk X-ray absorption spectrum for each of the three samples (LAX1, LAX2, and USC2) was separated into the XANES and EXAFS regions for analysis by LC fitting. The fit results give slightly different proportional mixtures of reference spectra for XANES *versus* EXAFS, but the reference components in the fit were the same for both. The bulk XAS spectra provide an estimate of the weighted atomic average of all major Fe species present in the sample. Results showed that the spectra were dominated overall by oxidized Fe(III) components, but other components with reduced oxidation states were also detected (Fig. 2; numerical fit results are shown in Table 2). Both LAX samples showed identical XANES spectra, irrespective of the collection period. The XANES features of the USC2 PM sample were slightly different from the LAX samples, particularly in the pre-edge region of the spectra (~7115 eV; Fig. 2A). In all spectra, the most abundant component was ferrihydrite (amorphous hydrous ferric oxide), which constituted from 34-52% of the total normalized Fe spectral signal considering both XANES and EXAFS fits (Fig. 2 and Table 2; see Fig. S3 for fit deconvolutions). Two other Fe oxide minerals, hematite (α-Fe_2O_3, Fe(III)-oxide) and magnetite (Fe_3O_4, mixed Fe(II,III)-oxide), were fit as major components, varying from 13-23% and 10-24%, respectively. An aluminosilicate component in the PM spectra was fit best with a reference spectrum of a natural mixed illite/smectite mineral, and varied from 16-23%. In addition, the USC2 sample showed a small but prominent contribution from metallic Fe(0) (2-6%), which gives rise to a distinctive absorption feature in the pre-edge XANES region (see Fig. S4). Evidence for the presence of Fe(0) was not found in the LAX samples in bulk spectra, but was identified in μ-XANES analyses (next section).

3.3 μ-XRF and μ-XANES

Spatially resolved Fe K-edge μ-XRF mapping (~2 μm spot size) of PM samples was used to locate regions with Fe fluorescence, and μ-XANES was collected at selected locations and deconvoluted with LC fits to identify the spectral components. These spatially resolved measurements were in general agreement with bulk XAS analyses but highlight the variability in the relative component fractions among different Fe hot spots. For example, a large area XRF map (600 x 300 μm) of the USC2 PM sample showed Fe fluorescence of variable intensity associated with particles throughout the sample, and a prominent spot ~20 μm in diameter (Fig. 3A). A μ-XANES spectrum acquired from this spot was notably different from spectra collected from other regions of the map. The distinctive pre-edge feature (~7115 eV) in the μ-XANES indicated the presence of a component with metallic Fe(0), which was about 30% of the spectral signal from LC fitting (Fig. 3B). Other components of the best fit were magnetite (6%) and ferrihydrite (61%), which may be partially (Fe(II,III)) and fully (Fe(III)) oxidized products, respectively, of the Fe(0) phase. Spectra collected from other locations had variable amounts of ferrihydrite, hematite, magnetite, illite/smectite, and Fe(0) (Fig. 3C; see Fig. S5A for additional spectra and LC fits). Other areas of the USC2 sample showed isolated Fe-rich areas in μ-XRF mapping that are probably particle aggregates based on electron microscopy (see below), but individual particles cannot be resolved with this technique (Fig. 3D and 3F). Analysis of μ-XANES of USC2 and LAX2 showed similar components present in different proportions, with spectra dominated by ferrihydrite (usually > 50%; see Fig. S5A), and lower abundances and variable amounts of the other components (Fig. 3E and 3G; Fig. S4). Fluorescence mapping of other transition metal elements in addition to Fe, together with μ-XANES analysis, showed some correlations. Copper and Zn were commonly associated with Fe-bearing particles (Fig. S5B), as was Ti and Mn with relatively lower intensity. In one example, a spot with a high fraction of Fe(0) (USC2_027) also showed relatively high amounts of Cr and Ni, characteristic of stainless steel (Fig. S5C) (Hedberg et al., 2013; Stockmann-Juvala et al., 2013).

3.4 STEM and EELS

Scanning transmission electron microscopy (STEM) was used to resolve particle morphologies, and EELS provided chemical and oxidation state information, at high spatial resolution (~ 1-5 nm). The relative intensity of Fe L_3 and L_2 peaks are sensitive to oxidation state (van Aken and Liebscher, 2002). Peak ratios of PM particle were compared with ratios of those from reference standards for Fe(0), Fe(II), Fe(II,III), and Fe(III) (Fig. S1). Because quantitative peak fits were limited by signal-to-noise, EELS spectra with clear L_3 and L_2 peaks were selected for analysis and thus biased towards particles with relatively high Fe.

Several morphological types were found for Fe-bearing particles. One characteristic morphology was 5-100 nm, sub-rounded or irregular particles clustered into larger aggregates (~50-500 nm) (e.g., LAX1 S1 and LAX S4 in Fig. 4A; see additional examples in Fig. S6). Particle Fe L_3/L_2 ratios (4.8-4.9) indicated average oxidation states lower than that of Fe(III) and magnetite (Fe(II,III). Some particles in this morphological class contained EELS peaks indicating the presence of Ti (LAX S4, Fig. 4A). Another distinctive particle morphology was highly spherical particles (20-100 nm) with Fe present as Fe(III) (L_3/L_2 =

5.7) and Mn present in lower abundance based on peak height relative to Fe (Fig. 4A; Fig. S6). A third prevalent particle morphology with Fe was layered particles with mostly irregular shapes that were sometimes transparent in STEM images, and with a relatively low Fe peak compared with O (Fig. 4A; Fig. S6). Analysis of Fe L_3/L_2 ratios indicated Fe oxidation states between Fe(II) and Fe(III).

Compared with the L_3/L_2 peak ratios of reference spectra overall, the EELS analyses of 12 particles showed ratios that were either similar to Fe(III) oxide compounds (ferrihydrite or hematite), or fell between Fe(III) and Fe(II) (Fig. 4B). Several particles had L_3/L_2 peak ratios that were similar to the ratio for Fe(II) (measured in ilmenite, $FeTiO_3$), and others were closer to or slightly lower than the ratio for magnetite. These results may indicate mixed oxidation states between Fe(III) and reduced Fe for some particles, while others are clearly Fe(III).

Particle STEM images coupled with elemental analyses by EDS line scans or points lend insight into particle compositions and potential sources. An Fe-oxide-rich particle with Ti, C, and Si but no Cu may be a brake wear fragment from an organic or polymer pad or lining (Fig. 5A), while an aggregated particle with high Cu but relatively low Fe, and with C and Si, is probably a wear product from a low-metallic or ceramic brake pad (Fig. 5B) (Sanders et al., 2003). Particles containing elevated Ba and S, probably from $BaSO_4$, together with Cu are a signature of brake pad wear fragments (Kukutschová and Filip, 2018; Sanders et al., 2003) (Fig. 5C). A particle was identified with high Zr and O, likely ZrO_2, with high Cu and no measurable Fe (Fig. 5D). This was also likely derived from brake wear as Zr is not a common element, and newer brake linings are using ZrO_2 and Cu nanoparticles in low-metallic formulations (Menapace et al., 2017).

3.5 STXM and EF-TEM

Carbon and Fe are two dominant components in PM, and their association and speciation was examined using spatially resolved C K-edge, O K-edge, and Fe L-edge STXM-XANES. STXM imaging of particles in the USC sample at the C absorption edge (288.5 eV) showed micrometer-sized particle aggregates (Fig. 6A). Carbon K-edge XANES of a particle aggregate showed characteristic aromatic C (~285 eV) and carboxylic acid C (~288.5 eV) absorbance features (Fig. 6B). Comparison of the PM XANES with spectra of synthetic C nanoparticles before and after chemical oxidation confirmed that the absorbance peak at 288.5 eV was associated with carboxylic acid (Moreno-Castilla et al., 1995; Pattammattel et al., 2019). Gaussian fitting of the C XANES PM spectra determined about 20% aromatic C, 72% carboxylic acid C, and 8% O-alkyl-C, which represents oxygen functional groups of organic compounds, as relative proportions of the spectra (Fig. S7). The O K-edge XANES (1s → empty states) collected from the same particle regions showed both carbonyl (1s → π_{CO}* transition at ~533 eV) and σ* (1s →2p σ* transition at ~540 eV) absorbance features that further confirm oxidation of the C surface (Fig. 6C). Interconnected spherical clusters (aciniform) of 30-50 nm C particles were observed in HR-TEM and STEM images, similar to the morphology of synthetic CNP (Fig. 6D) (Vander Wal et al., 2004). The concentric graphitic fringes in the spheres suggest its origin from a high temperature combustion process such as automobile engines (Li et al., 2011). For comparison to the STXM results,

an EELS spectrum of aggregated particles resolved both σ* and π* (1s →2p π*) transitions at the C K-edge, although the energy resolution is not high enough to resolve absorbances from specific functional groups (Fig. 6E). The chemistry of Fe associated with C-rich particles in PM was examined using C K- and Fe L-edge XANES spectra of a selected region from the C K-edge STXM map (Fig. S8). The Fe L-edge XANES collected over a 15 x 15 μm^2 area showed L_3 (~710 eV) and L_2 (~720 eV) peaks corresponding to an overall Fe(III) oxidation state. Iron associated with particles was heterogeneous and absorbance was weak, prohibiting quantitative speciation of individual regions due to poor signal to noise (Fig. S8C).

For comparison to the STXM data, energy filtered TEM (EF-TEM) images were collected at the C K- and Fe L- absorption edges (~2 nm spatial resolution; Fig. 6). At the C absorption energy, 20-30 nm spherical particles were resolved and C-rich regions were most prominent at 285 eV, the absorbance energy associated with aromatic C. Imaging the same particle at 710 eV showed Fe-rich regions, and indicated that Fe is both dispersed and localized in the C particles (Fig. 6). Localized Fe regions showed clusters of 10-20 nm nanoparticles with a strong Fe signal that were morphologically similar to those found in the STEM-EELS analyses above. Regions of low Fe intensity could be Fe(III) adsorbed on the oxidized C surface host.

4. Discussion

4.1 Oxidized and reduced forms of Fe in PM

In the urban $PM_{2.5}$ samples examined in this study, total Fe constituted a small fraction of the total sample mass (~40 μg/mg), but was present in multiple forms and oxidation states. Results from bulk XAS analyses of normalized spectra provided a quantitative assessment of the relative fractions of the major Fe species present in the PM samples because all Fe atoms in the sample contribute proportionally to the fluorescence signal. The average spectral signal from Fe was dominated by a component that was fit best with a ferrihydrite reference spectrum, comprising 34-52% of the total normalized Fe signal. Other major Fe phases identified by XAS analysis were hematite, magnetite, and illite/smectite, and a small fraction of Fe(0) (as Fe metal or stainless steel). Spatially resolved μ-XANES also indicated ferrihydrite as a major component in hot spot analyses, and best fits identified the same phases found as in bulk analyses but in different proportions among different particles. In STEM-EELS analyses of individual particles, the L_3/L_2 ratio for one set of particles was close to that of hematite and ferrihydrite (both Fe(III)), and other particles had Fe oxidation states intermediate between Fe(III) and Fe(II). High resolution EF-TEM images showed that Fe was present at relatively low concentrations across particles as well as concentrated in local areas associated with semi-spherical morphologies. These lines of evidence are consistent with a mixture of Fe phases dominated by Fe(III) (hydr)oxides (ferrihydrite and hematite), but with major fractions of magnetite and Fe-bearing illite/smectite. A portion of ferrihydrite appeared to be present as an oxidized or hydrated product of other Fe-rich phases associated with individual particles, which is expected as it is typically an oxidation and hydration product of crystalline Fe phases (Maxbauer et al., 2016; Schwertmann, 2008)., Spatially resolved methods showed that Fe was widespread on particles, perhaps as surface

nanoparticles that result from environmental oxidation, processing, and Fe hydroxide reprecipitation (Chen and Grassian, 2013; Nickovic et al., 2013; Shi et al., 2011). It should be noted that the fraction identified as ferrihydrite may also include some adsorbed Fe(III) as a hydroxo complex, which is difficult to detect in XAS mixtures because of its similarity to ferrihydrite in XANES and lack of backscattering features in EXAFS (Karlsson and Persson, 2010; Pattammattel et al., 2019). Our previous investigation using synthetic C nanoparticles with adsorbed Fe showed that Fe(III) formed either coordinated mononuclear surface complexes or ferrihydrite clusters on oxidized C surfaces, depending on the surface concentration of Fe(III) per unit area (Pattammattel et al., 2019).

Hematite (α-Fe_2O_3) was present on average in significant abundance (13-23%). Although hematite occurs naturally in soils, particularly in tropical regions, it is not abundant compared to goethite (α-FeOOH) and ferrihydrite in surface soils of temperate regions (Schwertmann, 2008). We compared XAS fits using spectra of naturally occurring hematite and nanocrystalline synthetic hematite (Fig. S9), and in all cases, XANES and EXAFS spectra were fit best with nanocrystalline synthetic hematite (particle size ~8 nm). In addition, particle sizes, morphologies, and association of Fe with C suggest that hematite is mostly of anthropogenic rather than geogenic origin (see next section). Goethite, which was identified in previous studies of PM using Mössbauer spectroscopy (Kopcewicz et al., 2015; Tavares et al., 2014; Weber et al., 2000) or TEM with SAED (Yang et al., 2016), and in Saharan dust samples using XAS (Formenti et al., 2014), was not identified in the bulk XAS fits. The Fe XANES spectra of goethite, hematite, and ferrihydrite can be similar and are slightly variable among samples of the same mineral type, depending on phase crystallinity and chemical impurities among natural and synthetic samples. The EXAFS spectra, however, are sufficiently different to distinguish among these Fe(III)-oxide phases if they comprise at least about 5% of the total atomic Fe absorption in the sample (Fig. S9) (O'Day et al., 2004).

The remaining two major fractions of Fe identified in bulk samples by XAS were magnetite (10-24%) and a phyllosilicate component best fit with a natural illite/smectite mineral (16-23%). Geologically, magnetite is a high temperature mineral found in igneous and metamorphic rocks. It is not common in surface environments where it is prone to oxidation; maghemite (γ -Fe_2O_3) has been observed as a surface oxidation product of magnetite (Maxbauer et al., 2016), but was not identified as a component of our samples. The presence of magnetite in PM of this study from an urban setting, and its association with carbonaceous material, indicates an anthropogenic origin (see next section). Phyllosilicate minerals (aluminosilicates with a layered sheet structure), in contrast, are common in soils and surface weathering environments where micaceous minerals such as illite, muscovite, and biotite alter to clay minerals of the smectite group (Brady and Weil, 2008). Among the set of reference spectra used to fit XAS data, we initially tested a number of different natural phyllosilicate minerals to represent the illite/smectite component. The best fits were consistently with a standard (IMt-1) that is dominated by illite, a mica mineral (Hower and Mowatt, 1966), rather than a soil clay mineral such as a Ca- or Na- smectite. Many soil phyllosilicate minerals have trace to low amounts of Fe along with other trace transition metal elements such Ti, V, Cr, Mn, Co, Ni, Cu, and Zn. However, phyllosilicate minerals, in particular vermiculite and some micas, are commonly used as filler material in commercial

brake pad and lining formulations (Thorpe and Harrison, 2008; Zhao et al., 2020). Anthropogenic and geogenic phyllosilicate sources of PM are discussed in the next section.

A minor but notable component identified by bulk and microfocused XAS was Fe(0) as metallic Fe (2-6% on average). Analysis of some particles by μ-XRF mapping and μ-XANES spectra showed high fractions of Fe(0) in a few particles, and the presence of trace Cr and Ni with Fe(0). A number of particles had EELS L_3/L_2 peak ratios that were below the ratio observed for magnetite, but higher than the ratio for Fe(II) or Fe(0). The observed ratios are consistent with mixtures or aggregates of nanoparticles of different phases, or with oxidation state differences between particle cores and surfaces that may reflect, for example, reduced particle cores and oxidized surfaces.

4.2 Sources of Fe in $PM_{2.5}$

Different forms of Fe in PM may originate from multiple anthropogenic or geogenic sources. Combustion and abrasion are the two primary anthropogenic processes in urban settings and near major roadways that generate PM-containing Fe and other metals (Luo et al., 2008; Muxworthy et al., 2002; Pant and Harrison, 2013; Sanderson et al., 2014; Sanderson et al., 2016). Wear products from braking systems (linings or pads, and rotors) are the major source of particle emissions from abrasion (Kukutschová and Filip, 2018), but abrasion products from engine wear are also emitted in exhaust and can be difficult to separate from combustion products. Direct knowledge of the chemical forms of Fe-bearing PM generated by emission sources before alteration by environmental processes comes primarily from laboratory studies of engine combustion products and abrasion materials.

4.2.1 Combustion emissions of Fe—Combustion-sourced Fe emissions from vehicles have been studied in engine exhaust or by using flame spray pyrolysis to simulate combustion, both with and without Fe-based fuel or lubricating oil additives such as ferrocene ($Fe(C_5H_5)_2$) or iron pentacarbonyl ($Fe(CO)_5$) (Bladt et al., 2012; Braun et al., 2006; Jasinski et al., 2006; Liati et al., 2015; Liati et al., 2013; Miller et al., 2007). Studies using an Fe additive in fuel that employed microscopic and/or spectroscopic characterizations of reaction products to determine product Fe phases identified hematite or maghemite (both Fe_2O_3 polymorphs) as products (Bladt et al., 2012; Braun et al., 2006; Jasinski et al., 2006), whereas another study inferred the presence of metallic Fe from particle morphology and engine temperature profile (Miller et al., 2007). In flame pyrolysis studies of Fe oxide nanoparticle formation, the particular Fe oxidation state and phases produced, which included maghemite, magnetite, and wustite (FeO), were controlled by the air to fuel ratio during combustion and the temperature, as well as the Fe additive used (Strobel and Pratsinis, 2009). Equilibrium phase relationships for the Fe-oxygen system show that hematite is the stable Fe oxide phase between about 400-1600° C under oxygenated (i.e., atmospheric) conditions, and magnetite (or wustite) is stable at lower oxygen partial pressures (Sundman, 1991). The experimental studies discussed above point to temperature and oxygen content as the primary variables that determine Fe phases produced in combustion, in overall agreement with equilibrium phase stability.

Our STEM-EELS data showed Fe-rich nanoparticles aggregated with carbonaceous materials and evidence of oxidized C functional groups. XAS analyses demonstrated the prevalence of hematite over magnetite, which may suggest combustion emissions at high temperature in oxygenated conditions as the primary hematite source. In studies of diesel exhaust without an additive, magnetite was identified as an Fe oxide product (Abdul-Razzaq and Gautam, 2001; Liati et al., 2015), but its source in one study was attributed to piston cylinder wear, high temperature melting in the engine, and subsequent cooling rather than combustion (Liati et al., 2015). A recent study of tailpipe emissions from 32 light-duty gasoline vehicles with a range of low emission certifications found that Fe in all samples was primarily Fe(III) except for two samples, one with Fe(0) and one with Fe(0) and Fe(III), and hematite and maghemite were detected as phases using Fe XANES (Salazar et al., 2020). While some magnetite might originate from diesel engines as indicated by older experimental studies (Abdul-Razzaq and Gautam, 2001), it is likely that diesel combustion as a source for magnetite has decreased with the advent of higher temperature, cleaner burning diesel engines, especially in California.

Highly spherical, Fe-bearing nanoparticles similar in morphology to those observed in our study have been reported previously in PM samples from Shanghai (China) and attributed to fly ash from coal combustion for electricity (Yang et al., 2016). The prevalent spherical particles observed in our samples contained oxidized Fe(III) and trace amounts of Mn, but not other trace elements (above EELS detection limits). A wide variety of trace elements have been identified in engine emissions (Gonet and Maher, 2019; Maricq, 2007), although most elements are present at very low concentrations in the absence of a fuel additive, and are not particularly diagnostic of source with the exception of the co-occurrence of V and Ni with Fe in heavy fuel oil (Streibel et al., 2017). Since there are no coal-fired power plants in California and prevailing winds are generally from the west and north-west, these spherical particles are likely derived from mobile combustion sources, but the specific sources are not known.

4.2.2 Abrasion emissions of Fe—Vehicular abrasion emissions of Fe are dominated by components of braking systems (Kukutschová and Filip, 2018). A wide variety of materials are used for linings and pads, which makes their identification in ambient PM challenging, whereas rotors are made mostly from gray cast Fe metal (Gramstat, 2018; Kukutschová and Filip, 2018; Osterle and Dmitriev, 2016). During braking events, brake pads heat up to between 100-400° C, with higher temperatures between 400-700° C observed for heavier vehicles under extreme conditions (Filip et al., 2002; Gramstat, 2018; Kukutschova et al., 2011). Repeated braking and high temperatures from frictional contact lead to the development of an altered layer (~0-5 μm) of variable thickness and roughness between the rotor and pad, which tends to thicken at higher temperatures (Filip et al., 2002; Osterle and Dmitriev, 2016). A review of brake wear studies concluded that the primary form of Fe in the friction layer was nanocrystalline magnetite mixed with graphite nanoparticles and other constituents from pad composite material (Osterle and Dmitriev, 2016). Magnetite, together with Fe(0) metal and hematite, were also reported in previous studies of PM generated by rail and subway systems, likely resulting from braking or contact between metal wheels and rails (Eom et al., 2013; Moreno et al., 2018). The temperature of

typical braking is consistent with oxidation of Fe(0) to magnetite as the stable iron oxide phase under moderately oxygenated conditions (Sundman, 1991). The irregular morphology of nano Fe-oxides observed here and in other STEM studies is consistent with an abrasion source such as braking (Kukutschova et al., 2011). Thus, brake wear is the most probable source for magnetite particles, which may undergo surface oxidation to hematite (or maghemite) or ferrihydrite.

Brake pad composition varies greatly across manufacturers among the common types in use, with organic and low-metallic pads typical of cars and light trucks, and semi-metallic pads used on heavy trucks. Pads often contain Fe as steel fibers or powders, or magnetite powder; metallic Cu and brass (CuZn alloy) are common additives in low-metallic and semi-metallic pad material (Kukutschová and Filip, 2018; Osterle and Dmitriev, 2016). Elevated Cu in particles relative to other elements is a signature of brake pad fragments (Sanders et al., 2003; Thorpe and Harrison, 2008). In our samples, clear indicators of brake pad wear fragments were the common association of Cu with Fe, high Cu concentration relative to Fe in some particle aggregates, and identification of $BaSO_4$ and ZrO_2 in particles. In a prior study of metal source apportionment in $PM_{2.5}$ from the same USC site as this study, Cu and Fe were attributed mostly to fresh traffic emissions, consistent with brake wear as a primary source (Mousavi et al., 2018).

Vermiculite or other micaceous phases are a major component of brake pad and lining fillers. Vermiculite is a natural mineral group that occurs as an alteration product of trioctahedral micas such as biotite and phlogopite, and is mined on a large scale from deposits interstratified with micaceous minerals such as biotite and chlorite that are higher in Fe than most soil smectites (Anthony et al., 2003; Society, 2019; Wang and Wang, 2019). Heating and abrasion of brake pads are known to dehydrate vermiculite (above ~200 °C) and convert it to a mica or talc-like phase (Filip et al., 2002). Conversion of vermiculite to mica or talc during brake pad heating and abrasion, and then potential mixing with ambient smectite-group minerals from soils, make it difficult to directly distinguish sources since these phases fall into the same mineral class (2:1 phyllosilicates) with similar crystal structures and XAS spectral signatures. The prevalence of mica rather than smectite in the XAS fits suggests a high fraction of micaceous phases derived from brake pad wear rather than a large component of soil-derived clay, although we cannot rule out a mixture from both sources.

A small but prominent fraction of Fe(0) was identified in bulk X-ray absorption spectra and in some high-Fe particles by μ-XANES. Detectable Cr was associated with Fe(0) in only 2 of 12 spot analyses and was not detected by EELS. The association of Cr with Fe(0) has been attributed to engine wear of steel components (Liati et al., 2015; Miller et al., 2007), and more recently with vapor deposition coatings of engine components using CrN and Cr_2N to improve engine performance and lifetime (Mehran et al., 2018). The lack of a Cr signature in most particles with Fe(0) may point to brake wear rather than engine wear as the primary source of Fe(0) particles. Abrasion of gray cast Fe from brake rotors would lack measurable Cr, and particles may be transformed by heat and pressure to magnetite and possibly hematite (Kukutschová and Filip, 2018; Osterle and Dmitriev, 2016).

5. Conclusions and implications

Based on bulk and spatially resolved data from multiple spectroscopy and microscopy characterization methods, Fe-bearing particles in PM samples can be attributed mostly to anthropogenic combustion or abrasion emissions, with little evidence for a large input from geogenic sources (i.e., soils or surface deposits). As determined from bulk XAS analyses, the largest Fe fraction (34-52%) was identified as ferrihydrite (amorphous Fe(III)-hydroxide), although this fraction may include some adsorbed Fe(III). Ferrihydrite can form as an oxidation or alteration product of any of the other Fe phases, either on particle surfaces or by dissolution and re-precipitation to form coatings or nanoparticles dispersed with carbonaceous materials and other phases. The prevalence of ferrihydrite (and/or related Fe hydroxide phases) and adsorbed Fe(III) has likely been underestimated in studies of ambient PM because it is non-crystalline, non-magnetic, more soluble than crystalline phases, and occurs in complex mixtures as surface coatings or nanoparticles. Environmental processes such as roadway abrasion or atmospheric processing during PM transport, especially in acidic conditions, will accelerate alteration of crystalline phases and produce ferrihydrite (Shi et al., 2012). Hematite (13-23%), in particular together with carbonaceous material, can form under oxygenated conditions at high temperature and was probably derived mostly from combustion processes (Salazar et al., 2020), which is dominantly vehicular near these collection sites but includes other sources (Shirmohammadi et al., 2017a). Magnetite (10-24%), and probably a fraction of hematite, likely originated mostly from brake wear from the frictional layer that forms between cast Fe rotors and pads or linings. The Fe-bearing phyllosilicate component (16-23%), which is best represented by an illite/smectite reference, was probably derived largely from vermiculite or other mica phases that are a major constituent of brake pad filler (Thorpe and Harrison, 2008; Zhao et al., 2020). Vermiculite dehydrates to a micaceous phase during brake heating (Filip et al., 2002), and then can weather, undergo grinding during road wear, and possibly mix with soil-derived clay minerals to constitute the illite/smectite fraction. Metallic Fe(0) was a relatively small (2-6%) but easily identified component, sometimes associated with Cr, and may have originated from either engine wear or brake systems.

The urban $PM_{2.5}$ samples of this study contain particles consisting of mixed Fe phases and oxidation states with variable morphologies, particle sizes, and aggregates, and association with carbonaceous material and a wide variety of trace elements. Although our samples provided a single, representative snapshot of Fe-bearing mixtures, spatial and temporal variation in component proportions at a given site is expected. In addition, the anthropogenic sources identified here of brake systems, fuels, and engines produce particles that have changed in composition over time and will change in the future. In general, no clear relationship has been established between bulk Fe concentration and health effects, although studies using model Fe particles have shown induction of inflammation, cytotoxicity, and genotoxicity to cells and animals (Arami et al., 2015; Ciğerci et al., 2018; Phumala et al., 1999; Valdiglesias et al., 2015). The variable mixtures that constitute urban PM have a high probability for electron transfer reactions between Fe and other redox-active metals such as Cu, and between these metals and reactive C species such as quinones. These types of reactions are associated with the production of hydrogen peroxide and hydroxyl radical that

induce oxidative stress (Charrier et al., 2014; Li et al., 2008). However, more subtle lipid peroxidation than is associated with oxidative stress can be initiated by Fe on the surface of silica resulting in the activation of pro-inflammatory signaling (Premasekharan et al., 2011). The oxidation state and association of Fe with particular phases are not currently considered in source apportionment and chemical speciation models, nor are they generally taken into account in cell or animal exposure studies. Knowledge of Fe chemical speciation can lead to the design and synthesis of model systems using engineered nanomaterials that reliably represent reactive particle mixtures in respirable PM.

Supplementary Material

Refer to Web version on PubMed Central for supplementary material.

Acknowledgements

Thanks to Dr. Jian Wang (Canadian Light Source) for his support and suggestions, and to Mengqiang (Mike) Zhu (University of Wyoming) and Xiaoming Wang (Huazhong Agricultural University, China) for providing the hematite EXAFS spectrum. We thank the UC Merced Imaging and Microscopy Facility and Mike Dunlap for the support in TEM studies, and thanks to U. Godwin Nwosu for assistance with data collection.

Funding

This work was supported by the National Institutes of Health (grant ES023864). Use of the Stanford Synchrotron Radiation Lightsource, SLAC National Accelerator Laboratory, is supported by the U.S. Department of Energy, Office of Science, Office of Basic Energy Sciences under Contract No. DE-AC02-76SF00515. Work at the Molecular Foundry was supported by the Office of Science, Office of Basic Energy Sciences, of the U.S. Department of Energy under Contract No. DE-AC02-05CH11231. A portion of the STXM data was acquired at the Canadian Light Source beamline10ID-1, which is supported by the NSERC, the CIHR, the NRC, and the University of Saskatchewan.

References

Abdul-Razzaq W, Gautam M, 2001 Discovery of magnetite in the exhausted material from a diesel engine. Appl. Phys. Lett 78, 2018–2019.

Anderson JO, Thundiyil JG, Stolbach A, 2012 Clearing the air: A review of the effects of particulate matter air pollution on human health. J. Med. Toxicol 8, 166–175. [PubMed: 22194192]

Anthony JW, Bideaux RA, Bladh KW, Nichols MC, 2003 Handbook of Mineralogy Mineralogical Society of America,, Chantilly, VA, USA.

Arami H, Khandhar A, Liggitt D, Krishnan KM, 2015 In vivo delivery, pharmacokinetics, biodistribution and toxicity of iron oxide nanoparticles. Chem. Soc. Rev 44, 8576–8607. [PubMed: 26390044]

Birch M, Cary R, 1996 Elemental carbon-based method for monitoring occupational exposures to particulate diesel exhaust. Aerosol Sci. Technol 25, 221–241.

Bladt H, Schmid J, Kireeva ED, Popovicheva OB, Perseantseva NM, Timofeev MA, Heister K, Uihlein J, Ivleva NP, Niessner R, 2012 Impact of Fe Content in Laboratory-Produced Soot Aerosol on its Composition, Structure, and Thermo-Chemical Properties. Aerosol Sci. Technol 46, 1337–1348.

Block ML, Calderon-Garciduenas L, 2009 Air pollution: mechanisms of neuroinflammation and CNS disease. Trends Neurosci. 32, 506–516. [PubMed: 19716187]

Brady NC, Weil RR, 2008 The Nature and Properties of Soils, 14th ed. Pearson Prentice Hall, Upper Saddle River, New Jersey.

Braun A, Huggins FE, Kelly KE, Mun BS, Ehrlich SN, Huffman GP, 2006 Impact of ferrocene on the structure of diesel exhaust soot as probed with wide-angle X-ray scattering and C(1s) NEXAFS spectroscopy. Carbon 44, 2904–2911.

Buzea C, Pacheco II, Robbie K, 2007 Nanomaterials and Nanoparticles: Sources and Toxicity. 2, MR17–MR71.

Cassee FR, Héroux M-E, Gerlofs-Nijland ME, Kelly FJ, 2013 Particulate matter beyond mass: recent health evidence on the role of fractions, chemical constituents and sources of emission. Inhal. Toxicol 25, 802–812. [PubMed: 24304307]

Charrier JG, McFall AS, Richards-Henderson NK, Anastasio C, 2014 Hydrogen Peroxide Formation in a Surrogate Lung Fluid by Transition Metals and Quinones Present in Particulate Matter. Environ. Sci. Technol 48, 7010–7017. [PubMed: 24857372]

Chen H, Grassian VH, 2013 Iron Dissolution of Dust Source Materials during Simulated Acidic Processing: The Effect of Sulfuric, Acetic, and Oxalic Acids. Environ. Sci. Technol 47, 10312–10321. [PubMed: 23883276]

Chen K-F, Lo S-C, Chang L, Egerton R, Kai J-J, Lin J-J, Chen F-R, 2007 Valence state map of iron oxide thin film obtained from electron spectroscopy imaging series. Micron 38, 354–361. [PubMed: 16934475]

Chow JC, Watson JG, 1999 Ion chromatography in elemental analysis of airborne particles, in: Landsberger S, Creatchman M (Eds.), Elemental Analysis of Airborne Particles. Gordon and Breach Science Publishers, pp. 97–137.

Ciğerci İH, Ali MM, Kaygısız ŞY, Kaya B, Liman R, 2018 Genotoxic assessment of different sizes of iron oxide nanoparticles and ionic iron in earthworm (Eisenia hortensis) coelomocytes by comet assay and micronucleus test. Bull. Environ. Contam. Toxicol 101, 105–109. [PubMed: 29802429]

Elzinga EJ, Gao Y, Fitts JP, Tappero R, 2011 Iron speciation in urban dust. Atmos. Environ 45, 4528–4532.

Eom HJ, Jung HJ, Sobanska S, Chung SG, Son YS, Kim JC, Sunwoo Y, Ro CU, 2013 Iron Speciation of Airborne Subway Particles by the Combined Use of Energy Dispersive Electron Probe X-ray Microanalysis and Raman Microspectrometry. Anal. Chem 85, 10424–10431. [PubMed: 24069900]

EPA, 2009 Integrated Science Assessment for Particulate Matter. U.S. EPA, Research Triangle Park, NC.

Filip P, Weiss Z, Rafaja D, 2002 On friction layer formation in polymer matrix composite materials for brake applications. Wear 252, 189–198.

Fine PM, Shen S, Sioutas C, 2004 Inferring the sources of fine and ultrafine particulate matter at downwind receptor sites in the Los Angeles basin using multiple continuous measurements. Aerosol Sci. Technol 38, 182–195.

Formenti P, Caquineau S, Chevaillier S, Klaver A, Desboeufs K, Rajot JL, Belin S, Briois V, 2014 Dominance of goethite over hematite in iron oxides of mineral dust from Western Africa: Quantitative partitioning by X-ray absorption spectroscopy. J. Geophys. Res.-Atmos 119, 12740–12754.

Gonet T, Maher BA, 2019 Airborne, Vehicle-Derived Fe-Bearing Nanoparticles in the Urban Environment: A Review. Environ. Sci. Technol 53, 9970–9991. [PubMed: 31381310]

Gramstat S, 2018 Chapter 10 - Technological Measures for Brake Wear Emission Reduction: Possible Improvement in Compositions and Technological Remediation: Cost Efficiency, in: Amato F (Ed.), Non-Exhaust Emissions. Academic Press, pp. 205–227.

Hedberg Y, Mazinanian N, Wallinder IO, 2013 Metal release from stainless steel powders and massive sheets - comparison and implication for risk assessment of alloys. Environ. Sci. Process. Imp 15, 381–392.

Hofman J, Maher BA, Muxworthy AR, Wuyts K, Castanheiro A, Samson R, 2017 Biomagnetic Monitoring of Atmospheric Pollution: A Review of Magnetic Signatures from Biological Sensors. Environ. Sci. Technol 51, 6648–6664. [PubMed: 28541679]

Hower J, Mowatt TC, 1966 The mineralogy of illites and mixed-layer illite/montmorillonites. Am. Mineral 51, 825–854.

Jasinski J, Pinkerton KE, Kennedy IM, Leppert VJ, 2006 Spatially resolved energy electron loss spectroscopy studies of iron oxide nanoparticles. Microscopy Microanal. 12, 424–431.

Karlsson T, Persson P, 2010 Coordination chemistry and hydrolysis of Fe(III) in a peat humic acid studied by X-ray absorption spectroscopy. Geochim. Cosmochim. Acta 74, 30–40.

Kopcewicz B, Kopcewicz M, Pietruczuk A, 2015 The Mossbauer study of atmospheric iron-containing aerosol in the coarse and PM2.5 fractions measured in rural site. Chemosphere 131, 9–16. [PubMed: 25765259]

Kukutschová J, Filip P, 2018 Chapter 6 - Review of Brake Wear Emissions: A Review of Brake Emission Measurement Studies: Identification of Gaps and Future Needs, in: Amato F (Ed.), Non-Exhaust Emissions. Academic Press, pp. 123–146.

Kukutschova J, Moravec P, Tomasek V, Matejka V, Smolik J, Schwarz J, Seidlerova J, Safarova K, Filip P, 2011 On airborne nano/micro-sized wear particles released from low-metallic automotive brakes. Environ. Poll 159, 998–1006.

Lerotic M, Mak R, Wirick S, Meirer F, Jacobsen C, 2014 MANTiS: a program for the analysis of X-ray spectromicroscopy data. J. Synchrotron Rad 21, 1206–1212.

Li N, Xia T, Nel AE, 2008 The role of oxidative stress in ambient particulate matter-induced lung diseases and its implications in the toxicity of engineered nanoparticles. Free Rad. Bio. Med 44, 1689–1699. [PubMed: 18313407]

Li Z, Song C, Song J, Lv G, Dong S, Zhao Z, 2011 Evolution of the nanostructure, fractal dimension and size of in-cylinder soot during diesel combustion process. Combust. Flame 158, 1624–1630.

Liati A, Pandurangi SS, Boulouchos K, Schreiber D, Arroyo Rojas Dasilva Y, 2015 Metal nanoparticles in diesel exhaust derived by in-cylinder melting of detached engine fragments. Atmos. Environ 101, 34–40.

Liati A, Schreiber D, Eggenschwiler PD, Dasilva YAR, 2013 Metal Particle Emissions in the Exhaust Stream of Diesel Engines: An Electron Microscope Study. Environ. Sci. Technol 47, 14495–14501. [PubMed: 24274188]

Luo C, Mahowald N, Bond T, Chuang PY, Artaxo P, Siefert R, Chen Y, Schauer J, 2008 Combustion iron distribution and deposition. Global Biogeochem. Cycles 22.

Majestic BJ, Schauer JJ, Shafer MM, 2007 Application of synchrotron radiation for measurement of iron red-ox speciation in atmospherically processed aerosols. Atmos. Chem. Phys 7, 2475–2487.

Maricq MM, 2007 Chemical characterization of particulate emissions from diesel engines: A review. J. Aerosol Sci 38, 1079–1118.

Maxbauer DP, Feinberg JM, Fox DL, 2016 Magnetic mineral assemblages in soils and paleosols as the basis for paleoprecipitation proxies: A review of magnetic methods and challenges. Earth-Sci. Rev 155, 28–48.

Mazzei F, D'alessandro A, Lucarelli F, Nava S, Prati P, Valli G, Vecchi R, 2008 Characterization of particulate matter sources in an urban environment. Sci. Tot. Environ 401, 81–89.

Mehran QM, Fazal MA, Bushroa AR, Rubaiee S, 2018 A Critical Review on Physical Vapor Deposition Coatings Applied on Different Engine Components. Crit. Rev. Solid State Mat. Sci 43, 158–175.

Menapace C, Leonardi M, Perricone G, Bortolotti M, Straffelini G, Gialanella S, 2017 Pin-on-disc study of brake friction materials with ball-milled nanostructured components. Mater. Design 115, 287–298.

Miller A, Ahlstrand G, Kittelson D, Zachariah M, 2007 The fate of metal (Fe) during diesel combustion: Morphology, chemistry, and formation pathways of nanoparticles. Combust. Flame 149, 129–143.

Misra C, Singh M, Shen S, Sioutas C, Hall PA, 2002 Development and evaluation of a personal cascade impactor sampler (PCIS). J. Aerosol Sci 33, 1027–1047.

Moreno T, Martins V, Reche C, Minguillón MC, de Miguel E, Querol X, 2018 Chapter 13 - Air Quality in Subway Systems, in: Amato F (Ed.), Non-Exhaust Emissions. Academic Press, pp. 289–321.

Moreno-Castilla C, Ferro-Garcia M, Joly J, Bautista-Toledo I, Carrasco-Marin F, Rivera-Utrilla J, 1995 Activated carbon surface modifications by nitric acid, hydrogen peroxide, and ammonium peroxydisulfate treatments. Langmuir 11, 4386–4392.

Mousavi A, Sowlat MH, Sioutas C, 2018 Diurnal and seasonal trends and source apportionment of redox-active metals in Los Angeles using a novel online metal monitor and Positive Matrix Factorization (PMF). Atmos. Environ 174, 15–24.

Muxworthy AR, Schmidbauer E, Petersen N, 2002 Magnetic properties and Mossbauer spectra of urban atmospheric particulate matter: a case study from Munich, Germany. Geophys. J. Int 150, 558–570.

Nickovic S, Vukovic A, Vujadinovic M, 2013 Atmospheric processing of iron carried by mineral dust. Atmos. Chem. Phys 13, 9169–9181.

O'Day PA, Rivera N, Root R, Carroll SA, 2004 X-ray absorption spectroscopic study of iron reference compounds for the analysis of natural sediments. Am. Mineral 89, 572–585.

Oakes M, Weber RJ, Lai B, Russell A, Ingall ED, 2012 Characterization of iron speciation in urban and rural single particles using XANES spectroscopy and micro X-ray fluorescence measurements: investigating the relationship between speciation and fractional iron solubility. Atmos. Chem. Phys 12, 745–756.

Osterle W, Dmitriev AI, 2016 The Role of Solid Lubricants for Brake Friction Materials. Lubricants 4, 22.

Pant P, Harrison RM, 2013 Estimation of the contribution of road traffic emissions to particulate matter concentrations from field measurements: A review. Atmos. Environ 77, 78–97.

Pattammattel A, Leppert VJ, Forman HJ, O'Day PA, 2019 Surface characterization and chemical speciation of adsorbed iron(III) on oxidized carbon nanoparticles. Environ. Sci. Process. Imp 21, 548–563.

Petroselli C, Moroni B, Crocchianti S, Selvaggi R, Vivani R, Soggia F, Grotti M, d'Acapito F, Cappelletti D, 2019 Iron Speciation of Natural and Anthropogenic Dust by Spectroscopic and Chemical Methods. Atmosphere 10, 15.

Phumala N, Ide T, Utsumi H, 1999 Noninvasive evaluation of in vivo free radical reactions catalyzed by iron using in vivo ESR spectroscopy. Free Rad. Bio. Med 26, 1209–1217. [PubMed: 10381192]

Premasekharan G, Nguyen K, Contreras J, Ramon V, Leppert VJ, Forman HJ, 2011 Iron-mediated lipid peroxidation and lipid raft disruption in low-dose silica-induced macrophage cytokine production. Free Rad. Bio. Med 51, 1184–1194. [PubMed: 21741475]

Ravel B, Newville M, 2005 "ATHENA, ARTEMIS, HEPHAESTUS: Data analysis for X-ray absorption spectroscopy using IFEFFIT" J. Synchrotron Rad, 537–541.

Roberts AP, Heslop D, Zhao X, Pike CR, 2014 Understanding fine magnetic particle systems through use of first-order reversal curve diagrams. Rev. Geophys 52, 557–602.

Salazar JR, Cartledge BT, Haynes JP, York-Marini R, Robinson AL, Drozd GT, Goldstein AH, Fakra SC, Majestic BJ, 2020 Water-soluble iron emitted from vehicle exhaust is linked to primary speciated organic compounds. Atmos. Chem. Phys 20, 1849–1860.

Sanders PG, Xu N, Dalka TM, Maricq MM, 2003 Airborne brake wear debris: Size distributions, composition, and a comparison of dynamometer and vehicle tests. Environ. Sci. Technol 37, 4060–4069. [PubMed: 14524436]

Sanderson P, Delgado-Saborit JM, Harrison RM, 2014 A review of chemical and physical characterisation of atmospheric metallic nanoparticles. Atmos. Environ 94, 353–365.

Sanderson P, Su SS, Chang ITH, Saborit JMD, Kepaptsoglou DM, Weber RJM, Harrison RM, 2016 Characterisation of iron-rich atmospheric submicrometre particles in the roadside environment. Atmos. Environ 140, 167–175.

Schauer JJ, Rogge WF, Hildemann LM, Mazurek MA, Cass GR, Simoneit BRT, 1996 Source apportionment of airborne particulate matter using organic compounds as tracers. Atmos. Environ 30, 3837–3855.

Schwertmann U, 2008 Iron Oxides, in: Chesworth W (Ed.), Encyclopedia of Soil Science. Springer, pp. 363–369.

Schwertmann U, Cornell RM, 2000 Iron Oxides in the Laboratory: Preparation and Characterization, Second Edition. Wiley-VCH.

See SW, Wang YH, Balasubramanian R, 2007 Contrasting reactive oxygen species and transition metal concentrations in combustion aerosols. Environ. Res 103, 317–324. [PubMed: 17011545]

Shi Z, Bonneville S, Krom MD, Carslaw KS, Jickells TD, Baker AR, Benning LG, 2011 Iron dissolution kinetics of mineral dust at low pH during simulated atmospheric processing. Atmos. Chem. Phys 11, 995–1007.

Shi ZB, Krom MD, Jickells TD, Bonneville S, Carslaw KS, Mihalopoulos N, Baker AR, Benning LG, 2012 Impacts on iron solubility in the mineral dust by processes in the source region and the atmosphere: A review. Aeolian Res. 5, 21–42.

Shirmohammadi F, Lovett C, Sowlat MH, Mousavi A, Verma V, Shafer MM, Schauer JJ, Sioutas C, 2018 Chemical composition and redox activity of PM0.25 near Los Angeles International Airport and comparisons to an urban traffic site. Sci. Tot. Environ 610, 1336–1346.

Shirmohammadi F, Sowlat MH, Hasheminassab S, Saffari A, Ban-Weiss G, Sioutas C, 2017a Emission rates of particle number, mass and black carbon by the Los Angeles International Airport (LAX) and its impact on air quality in Los Angeles. Atmos. Environ 151, 82–93.

Shirmohammadi F, Wang D, Hasheminassab S, Verma V, Schauer JJ, Shafer MM, Sioutas C, 2017b Oxidative potential of on-road fine particulate matter (PM2.5) measured on major freeways of Los Angeles, CA, and a 10-year comparison with earlier roadside studies. Atmos. Environ 148, 102–114.

Society CM, 2019 The Clay Minerals Society Glossary of Clay Science. The Clay Minerals Society, Chantilly, VA.

Stockmann-Juvala H, Hedberg Y, Dhinsa NK, Griffiths DR, Brooks PN, Zitting A, Wallinder IO, Santonen T, 2013 Inhalation toxicity of 316L stainless steel powder in relation to bioaccessibility. Human Exper. Toxicol 32, 1137–1154.

Streibel T, Schnelle-Kreis J, Czech H, Harndorf H, Jakobi G, Jokiniemi J, Karg E, Lintelmann J, Matuschek G, Michalke B, Muller L, Orasche J, Passig J, Radischat C, Rabe R, Reda A, Ruger C, Schwemer T, Sippula O, Stengel B, Sklorz M, Torvela T, Weggler B, Zimmermann R, 2017 Aerosol emissions of a ship diesel engine operated with diesel fuel or heavy fuel oil. Environ. Sci. Poll. Res 24, 10976–10991.

Strobel R, Pratsinis SE, 2009 Direct synthesis of maghemite, magnetite and wustite nanoparticles by flame spray pyrolysis. Adv. Powder Technol 20, 190–194.

Sundman B, 1991 An assessment of the Fe-O system. J. Phase Equil 12, 127–140.

Tao F, Gonzalez-Flecha B, Kobzik L, 2003 Reactive oxygen species in pulmonary inflammation by ambient particulates. Free Rad. Bio. Med 35, 327–340. [PubMed: 12899936]

Tavares FVF, Ardisson JD, Rodrigues PCH, Brito W, Macedo WAA, Jacomino VMF, 2014 Characterization of iron in airborne particulate matter. Hyperfine Interact. 224, 109–119.

Thorpe A, Harrison RM, 2008 Sources and properties of non-exhaust particulate matter from road traffic: A review. Sci. Tot. Environ 400, 270–282.

Valdiglesias V, Kiliç G, Costa C, Fernández-Bertólez N, Pásaro E, Teixeira JP, Laffon B, 2015 Effects of iron oxide nanoparticles: cytotoxicity, genotoxicity, developmental toxicity, and neurotoxicity. Environ. Molec. Mutagen 56, 125–148. [PubMed: 25209650]

van Aken PA, Liebscher B, 2002 Quantification of ferrous/ferric ratios in minerals: new evaluation schemes of Fe L-23 electron energy-loss near-edge spectra. Phys. Chem. Miner 29, 188–200.

Vander Wal RL, Tomasek AJ, Street K, Hull DR, Thompson WK, 2004 Carbon nanostructure examined by lattice fringe analysis of high-resolution transmission electron microscopy images. Appl. Spectros 58, 230–237.

Wang W, Wang A, 2019 9 - Vermiculite Nanomaterials: Structure, Properties, and Potential Applications, in: Wang A, Wang W (Eds.), Nanomaterials from Clay Minerals. Elsevier, pp. 415–484.

Webb SM, 2005 SIXpack: a graphical user interface for XAS analysis using IFEFFIT. Phys. Scr T115, 1011–1014.

Weber S, Hoffmann P, Ensling J, Dedik AN, Weinbruch S, Miehe G, Gutlich P, Ortner HM, 2000 Characterization of iron compounds from urban and rural aerosol sources. J. Aerosol Sci 31, 987–997.

WHO, 2016 Ambient air pollution: A global assessment of exposure and burden of disease. World Health Organization, Geneva, Switzerland, p. 131.

Yang Y, Vance M, Tou FY, Tiwari A, Liu M, Hochella MF, 2016 Nanoparticles in road dust from impervious urban surfaces: distribution, identification, and environmental implications. Environ. Sci. Nano 3, 534–544.

Yazdani F, Seddigh M, 2016 Magnetite nanoparticles synthesized by co-precipitation method: The effects of various iron anions on specifications. Mater. Chem. Phys 184, 318–323.

Zhao XG, Ouyang J, Tan Q, Tan XM, Yang HM, 2020 Interfacial characteristics between mineral fillers and phenolic resin in friction materials. Mater. Exp 10, 70–80.

Highlights

- Multi-method spectro-microscopy characterization of iron (Fe) speciation in $PM_{2.5}$
- Ferrihydrite (amorphous Fe(III)-hydroxide) comprised the largest Fe fraction
- Hematite, magnetite, and Fe in phyllosilicates were major crystalline components
- Mixed Fe phases and oxidation states often associated with carbonaceous material
- Fe-bearing PM mostly from anthropogenic sources (brake wear and exhaust products)

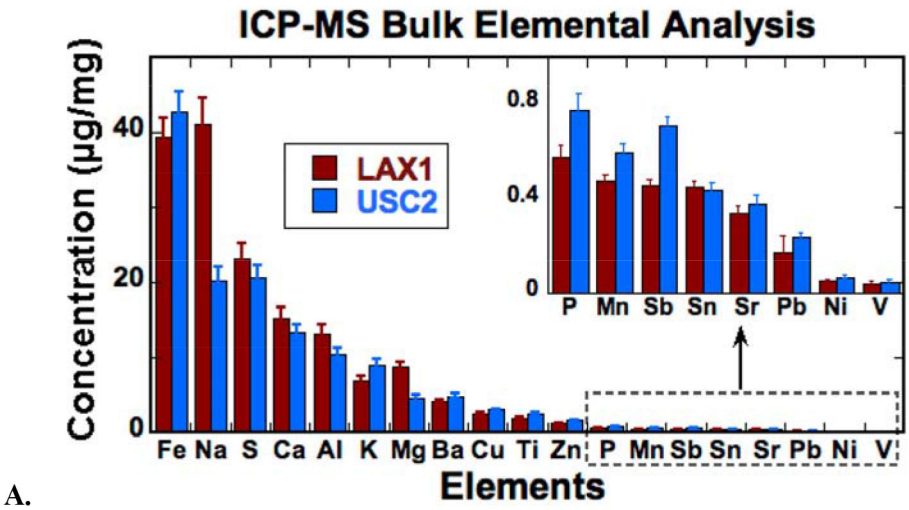

A.

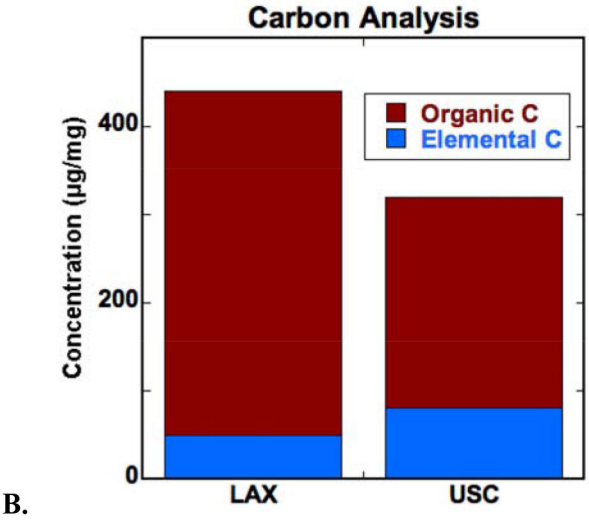

B.

Figure 1.

Bulk chemical analysis of $PM_{2.5}$ samples filters LAX1 and USC2 from replicate filters: **A.** Elemental analysis by ICP-MS; **B.** Concentrations of elemental and organic carbon (C).

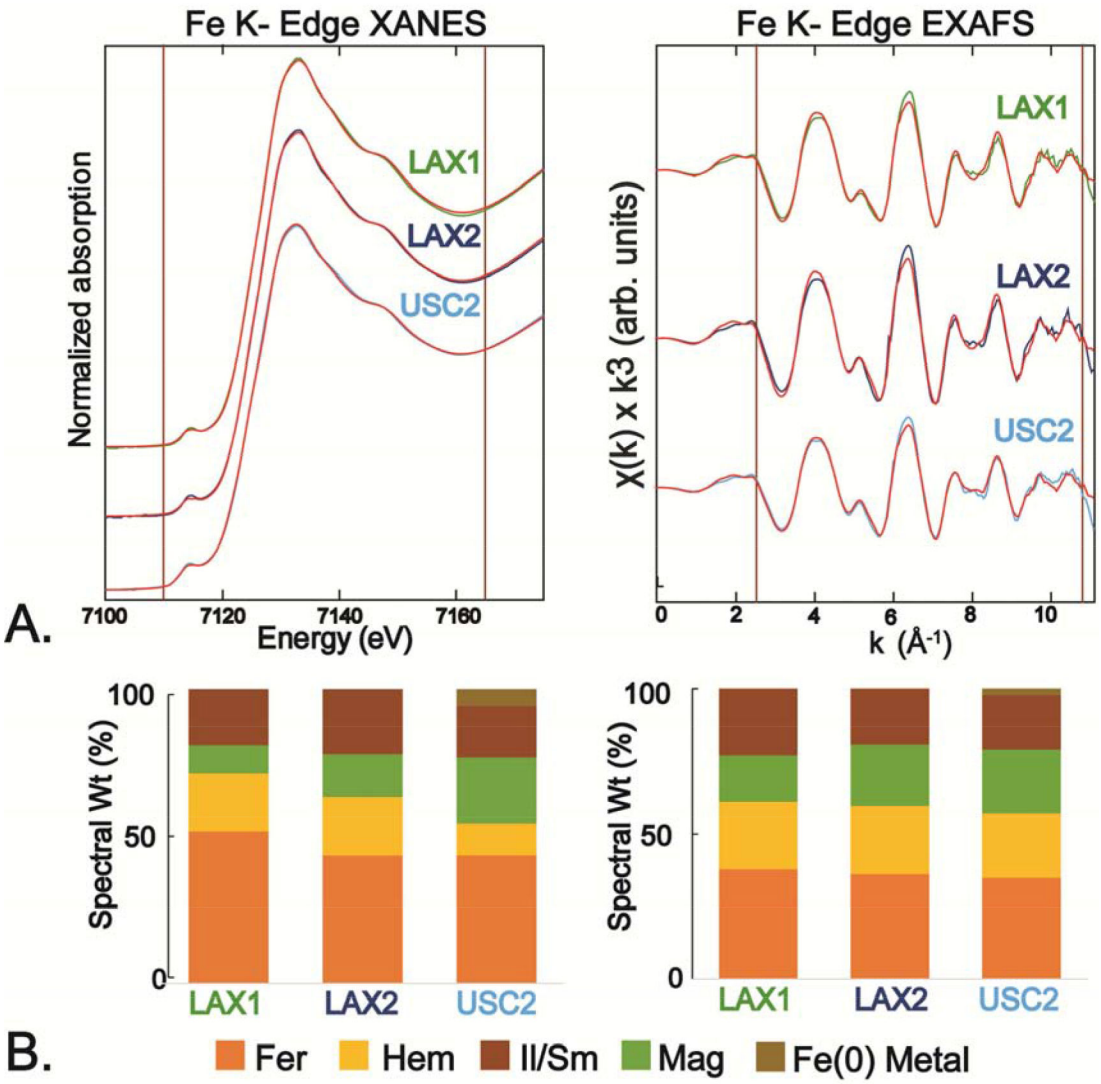

Figure 2.

A. Iron K-edge XANES and EXAFS of ambient $PM_{2.5}$ samples and their linear combination (LC) best fits (in red); see Fig. S1 for fit deconvolutions with individual reference spectra. **B.** Relative percentages of individual components determined from LC fits of XANES and EXAFS with reference spectra (normalized to 100%). Numerical fit results are given in Table 2. Abbreviations: Fer - ferrihydrite (am-$Fe(OH)_3$); Hem - hematite (α-Fe_2O_3); Mag - magnetite (Fe_3O_4); Il/Sm – illite/smectite (Clay Minerals Society IMt-1); see Table S2 for details of reference compound spectra.

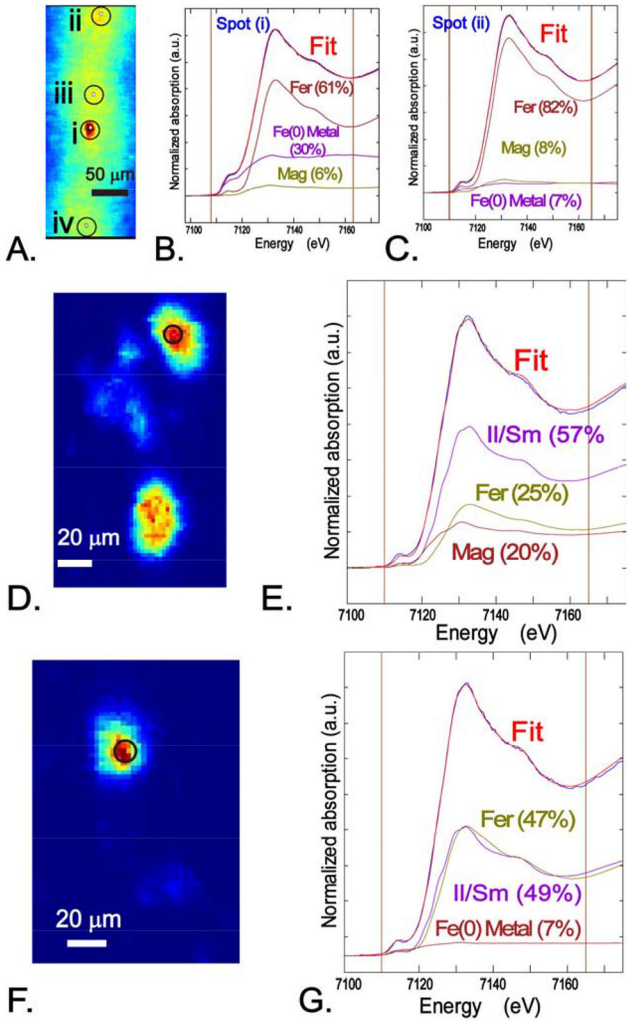

Figure 3.

Microfocused X-ray fluorescence (μ-XRF) maps and μ-XANES with linear combination (LC) fits with reference spectra from sample USC2. **A.** Fe Kα map of a large region showing Fe intensity (red tones). μ-XANES and LC fits from **B.** spot (i) and **C.** spot (ii). **D-F**. μ-XRF of particle aggregates and LC fits of μ-XANES spectra collected the areas indicated. Abbreviations: Fer - ferrihydrite (am-$Fe(OH)_3$); Fe(0) Metal - ground Fe metal; Mag - magnetite (Fe_3O_4); Il/Sm – illite/smectite (Clay Minerals Society IMt-1); see Table S2 for details of reference compound spectra.

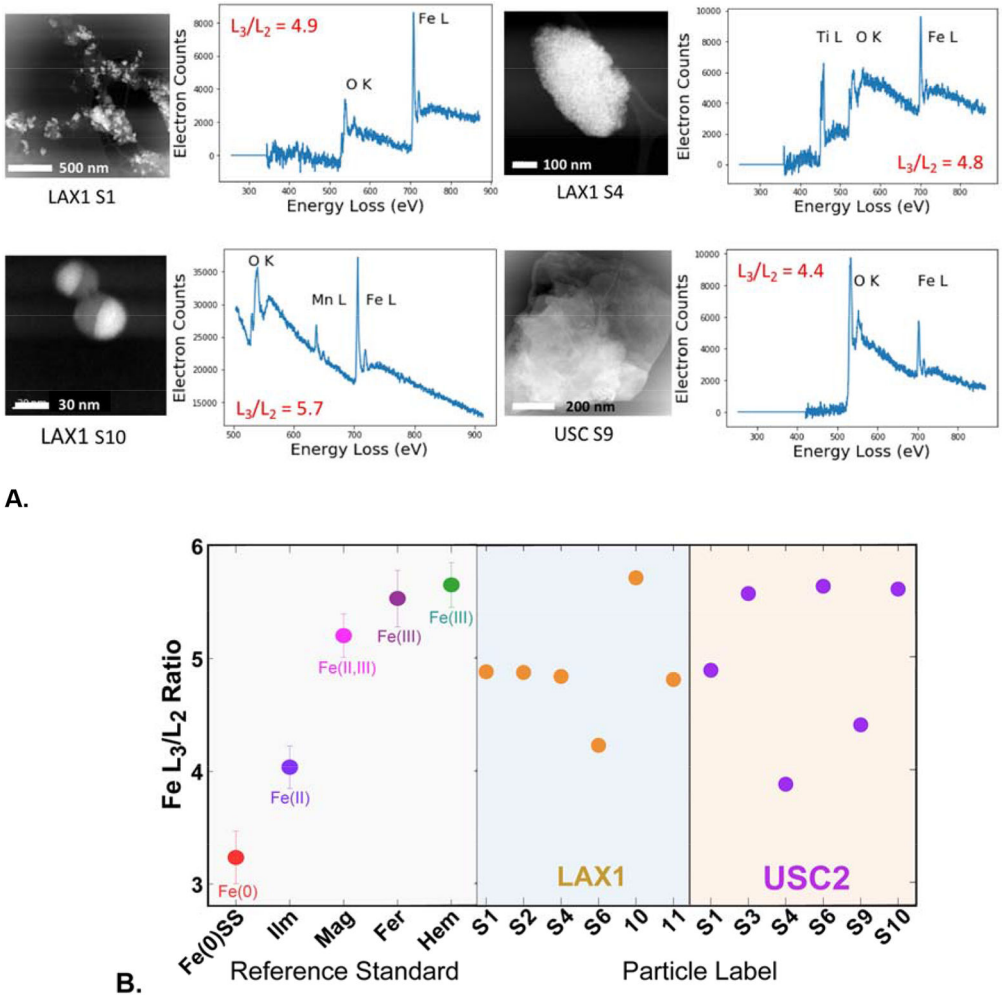

Figure 4.

Spatially resolved Fe L_3/L_2-edge electron energy loss spectroscopy (EELS) of LAX1 and USC2 samples. **A**. Representative STEM images and EELS spectra (background subtracted) of particle morphologies; see Fig. S6 for additional STEM images. **B**. Summary of L_3/L_2 ratios of Fe-rich PM particles compared with ratios of reference standards. Error bars represent the standard deviation of multiple measurements of reference standards (n > 6). Abbreviations: Fe(0)SS - stainless steel nanoparticles; Ilm - ilmenite ($FeTiO_3$); Mag - magnetite (Fe_3O_4); Fer - ferrihydrite (am-$Fe(OH)_3$); Hem - hematite (α-Fe_2O_3); see Fig. S1 and Table S3 for details of reference compound spectra.

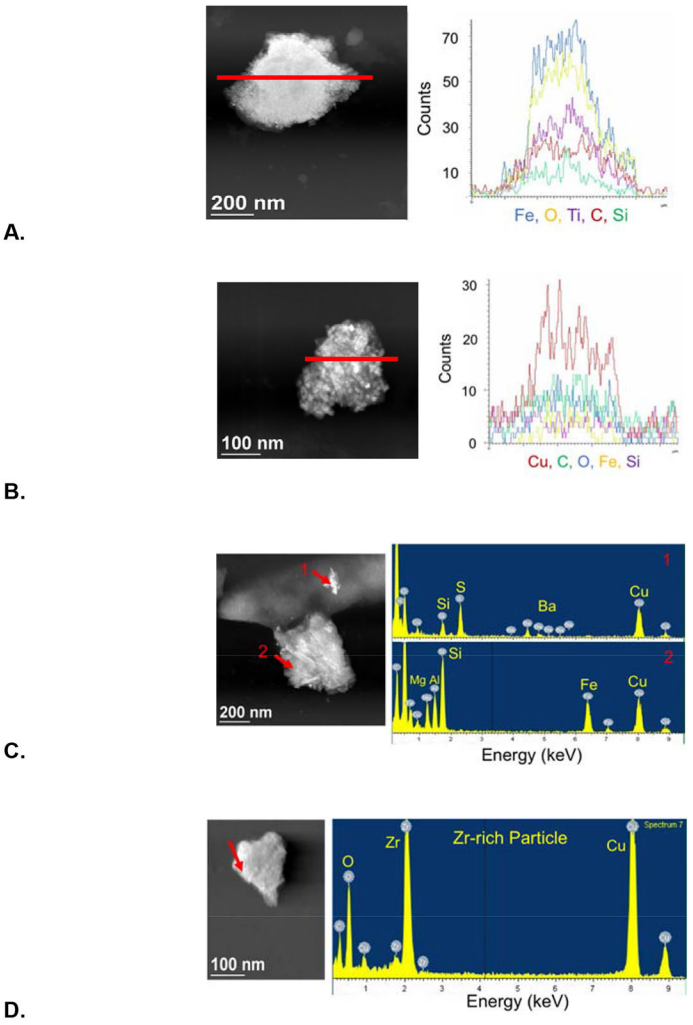

Figure 5.

Scanning transmission electron microscopy (STEM) image and energy dispersive spectrometry (EDS) line scan (red line) or point analysis (red arrow) of: **A.** Fe-oxide and Ti-rich particle with C and Si; **B.** Aggregate particle with high Cu, C and Si, and relatively low Fe; **C.** Two particles, (1) one with Ba and S, likely BaSO4, and Cu, and (2) one with Fe, Cu, and Si, and lower amounts of Mg and Al; **D.** Zr- and O- rich particle, likely ZrO_2, with Cu.

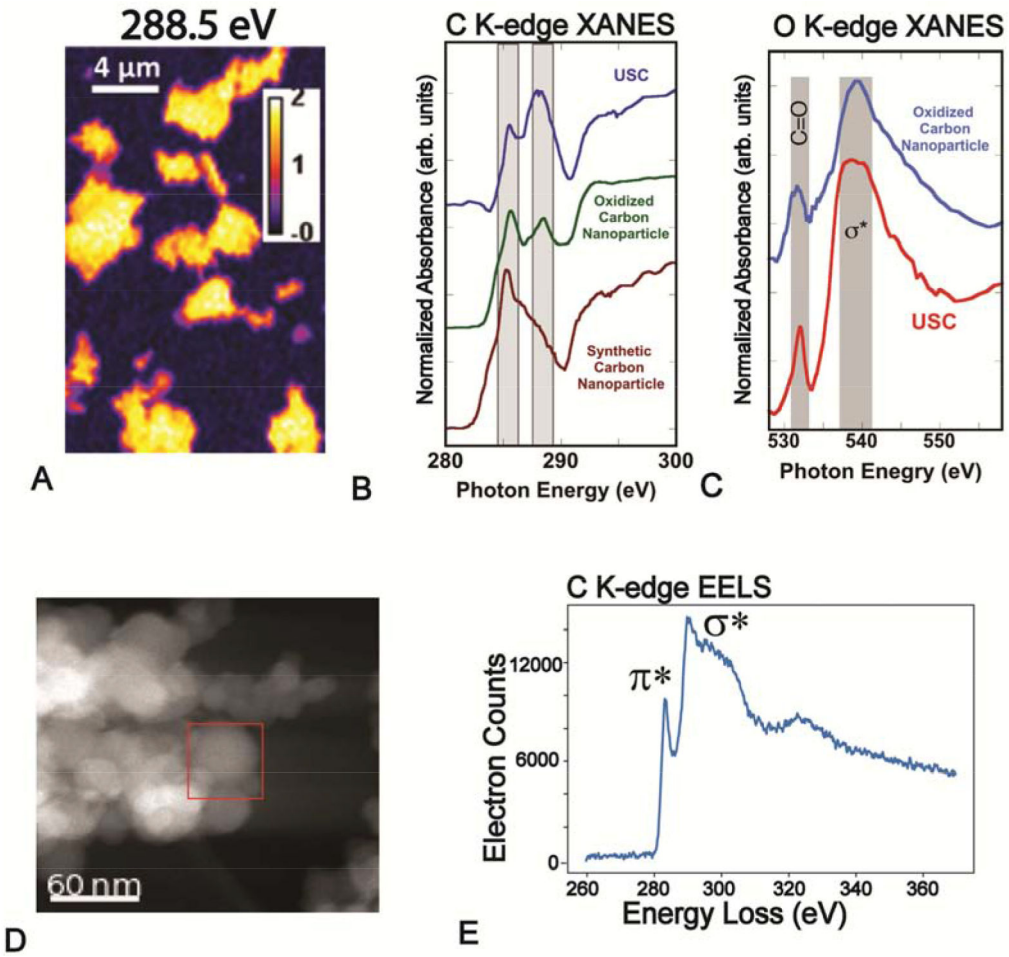

Figure 6.

Characterizations of C-rich particles from sample USC: **A.** Carbon K-edge scanning transmission X-ray microscopy (STXM) image of ambient PM at 288.5 eV. **B.** Integrated carbon K-edge XANES of ambient PM from STXM image (A) compared with reference spectra of untreated and chemically oxidized synthetic carbon nanoparticles (CNP). **C.** O K-edge XANES of PM from the same region compared with a reference spectrum of oxidized synthetic CNP. **D**. STEM image of C-rich particles. **E**. Corresponding C K-edge EELS spectrum from area marked in D.

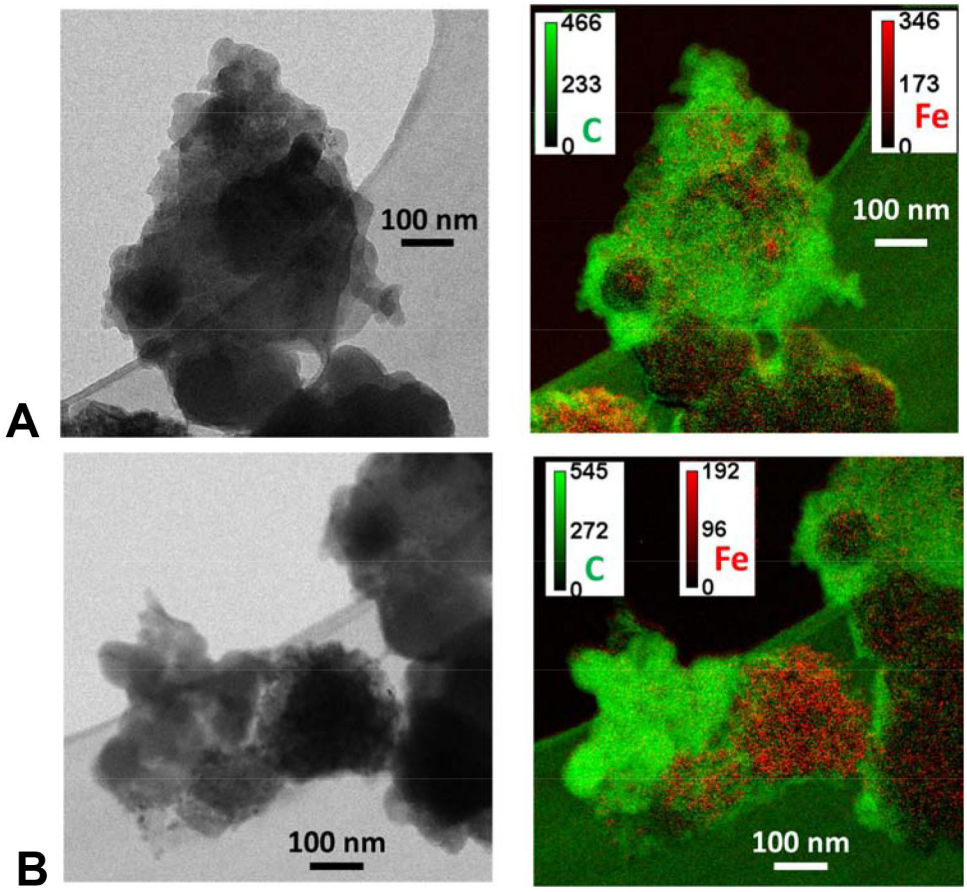

Figure 7.

A and B. Representatitive transmission electron microscopy (TEM) images and composite energy filterd-TEM (EF-TEM) images of Fe associated with C particles. Calibration bar shows the electron counts per second.

Table 1.

Sampling periods and masses of $PM_{2.5}$ samples used in this study.

Sample[a]	Sampling period	Mass (μg)
LAX1	11/10/2016-11/17/2016	420.0
LAX2	11/24/2016-12/02/2016	268.5
USC1	11/24/2016-12/02/2016	436.0
USC2	11/10/2016-11/17/2016	293.5

[a]LAX: Los Angeles Airport site; USC: University of Southern California site.

Table 2.

Linear combination fit results from Fe K-edge XANES and EXAFS.

	XANES (E range 7110-7165 eV)			EXAFS (k range 2.5-10.8 Å^{-1})	
Sample	**Standard** [a]	**Fit % (±)** [b]	**Normalized %**	**Fit % (±)** [b]	**Normalized %**
LAX1	Fer	51.3 (1.8)	51.8	41.8 (2.5)	37.9
	Hem	19.5 (2.2)	19.7	25.6 (0.9)	23.2
	Mag	9.5 (0.7)	9.6	17.8 (1.7)	16.1
	Il/Sm	18.8 (2.0)	19	25.3 (2.2)	22.9
	Sum	*99.0*		*110.4*	
	R-factor [c]	*0.0001346*		*0.0202*	
	Red. χ^2 [d]	*0.0000349*		*0.144*	
LAX2	Fer	43.2 (1.6)	43.5	39.7 (2.7)	36.2
	Hem	19.7 (2.1)	19.9	25.7 (1.0)	23.4
	Mag	14.5 (0.6)	14.6	23.4 (1.8)	21.3
	Il/Sm	21.8 (1.9)	22.0	21.0 (2.3)	19.1
	Sum	*99.2*		*109.8*	
	R-factor [c]	*0.000118*		*0.0244*	
	Red. χ^2 [d]	*0.0000298*		*0.168*	
USC2	Fer	41.7 (2.4)	42.1	35.0 (2.3)	34.2
	Hem	12.5 (2.6)	12.6	22.9 (0.8)	22.4
	Mag	22.8 (1.9)	23.0	24.4 (1.4)	23.9
	Il/Sm	16.4 (3.3)	16.5	17.7 (1.9)	17.3
	Fe(0) Metal	5.7 (0.7)	5.8	2.3 (0.4)	2.2
	Sum	*99.1*		*102.3*	
	R-factor [c]	*0.000236*		*0.0183*	
	Red. χ^2 [d]	*0.0000542*		*0.106*	

[a] Abbreviations: Fer - Ferrihydrite, Hem - Hematite, Mag - Magnetite, Il/Sm – Illite/smectite. See Table S2 for details of reference compound spectra.

[b] Estimated uncertainties (in parentheses) are from statistical fit results only.

[c] R-factor = $\Sigma(\text{data-fit})^2 / \Sigma(\text{data})^2$ -- normalized sum of squared residuals of the fit.

[d] Reduced χ^2 = R-factor / (# of points - # of variables) -- goodness of fit parameter accounting for the number of variables in the fit.